Rotation and Neoclassical Ripple Transport in ITER

E. J. Paul,[1] M. Landreman,[2] W. Dorland,[1] F. M. Poli,[3] D. A. Spong,[4] and H. M. Smith[5]

[1] *Department of Physics, University of Maryland, College Park, MD 20742,*
USA[a)]

[2] *Institute for Research in Electronics and Applied Physics, University of Maryland,*
College Park, MD 20742, USA[b)]

[3] *Princeton Plasma Physics Laboratory, Princeton, NJ 08543,*
USA[c)]

[4] *Oak Ridge National Laboratory, Oak Ridge, TN 37831,*
USA[d)]

[5] *Max-Planck-Institut für Plasmaphysik, 17491 Greifswald,*
Germany[e)]

Neoclassical transport in the presence of non-axisymmetric magnetic fields causes a toroidal torque known as neoclassical toroidal viscosity (NTV). The toroidal symmetry of ITER will be broken by the finite number of toroidal field coils and by test blanket modules (TBMs). The addition of ferritic inserts (FIs) will decrease the magnitude of the toroidal field ripple. 3D magnetic equilibria in the presence of toroidal field ripple and ferromagnetic structures are calculated for an ITER steady-state scenario using the Variational Moments Equilibrium Code (VMEC). Neoclassical transport quantities in the presence of these error fields are calculated using the Stellarator Fokker-Planck Iterative Neoclassical Conservative Solver (SFINCS). These calculations fully account for E_r, flux surface shaping, multiple species, and collisionality rather than applying analytic NTV formulae. As NTV is a complicated nonlinear function of E_r, we study its behavior over a plausible range of E_r. We estimate the toroidal flow, and hence E_r, using a semi-analytic turbulent intrinsic rotation model and NUBEAM calculations of neutral beam torque. The magnitude of NTV torque density at large radii ($r/a \gtrsim 0.6$) is comparable to the NBI torque density at small radii ($r/a \lesssim 0.4$), but is opposite in direction and may significantly damp rotation in the edge. The NTV from the $n = 18$ perturbation dominates that from lower n perturbations of the TBMs.

———————

[a] Electronic mail: ejpaul@umd.edu

[b] Electronic mail: mattland@umd.edu

[c] Electronic mail: fpoli@pppl.gov

[d] Electronic mail: spongda@ornl.gov

[e] Electronic mail: hakan.smith@ipp.mpg.de

I.   INTRODUCTION

Toroidal rotation is critical to the experimental control of tokamaks: the magnitude of rotation is known to suppress resistive wall modes,[1,2] while rotation shear can decrease microinstabilities and promote formation of transport barriers.[3,4] As some ITER scenarios will be above the no-wall stability limit,[5] it is important to understand the sources and sinks of angular momentum for stabilization of external kink modes. One such sink (or possibly source) is the toroidal torque caused by 3D non-resonant error fields, known as neoclassical toroidal viscosity (NTV). Dedicated NTV experiments have been conducted in the Mega Amp Spherical Tokamak (MAST),[6] the Joint European Tokamak (JET),[7,8] Alcator C-MOD,[9] DIII-D,[10,11] JT-60U,[12] and the National Spherical Tokamak Experiment (NSTX).[13]

In addition to the ripple due to the finite number (18) of toroidal field (TF) coils, the magnetic field in ITER will be perturbed by ferromagnetic components including ferritic inserts (FIs) and test blanket modules (TBMs). TBMs will be installed in three equatorial ports to test tritium breeding and extraction of heat from the blanket. The structural material for these modules is ferritic steel and will produce additional error fields in response to the background field. The TBMs will be installed during the H/He phase in order to test their performance in addition to their possible effects on confinement and transport.[14] It is important to understand their effect on transport during the early phases of ITER, including their influence on angular momentum transport. Experiments at DIII-D using mock-ups of TBMs found a reduction in toroidal rotation by as much as 60% due to an $n = 1$ locked mode.[15] Here n is the toroidal mode number. Compensation by $n = 1$ control coils enable access to low NBI torque (1.1 Nm) regimes relevant to ITER without rotation collapse.[16] In addition to TBMs, ferritic steel plates will be installed in each of the toroidal field coil sections in order to mitigate energetic particle loss due to TF ripple.[17] As FIs will decrease toroidal field ripple, they may decrease the NTV in ITER. Experiments including FIs on JT-60U[18] and JFT-2M[19] have found a reduction in counter-current rotation with the addition of FIs.

While the bounce-averaged radial drift vanishes in a tokamak, trapped particles may wander off the flux surface in the presence of non-axisymmetric error fields. Particles trapped

poloidally can drift radially as the parallel adiabatic invariant, $J_{||} = \oint v_{||} dl$, becomes a function of toroidal angle in broken symmetry. Here $v_{||}$ is the velocity coordinate along $\boldsymbol{b} = \boldsymbol{B}/B$ and integration is taken along the field between bounce points. If local ripple wells exist along a field line and the collisionality is small enough that helically trapped particles can complete their collisionless orbits, these trapped particles may grad-B drift away from the flux surface.[20] For a general electric field, the electron and ion fluxes are not necessarily identical. As ambipolarity must be restored for charge conservation, a radial electric field develops to hold the ions back. The radial current caused by outward ion flow induces a $\boldsymbol{J} \times \boldsymbol{B}$ torque which is typically counter-current.

Analytic expressions for neoclassical fluxes in several rippled tokamak regimes have been derived, making assumptions about the magnitude of the perturbing field, electric field, magnetic geometry, collisionality, and the collision operator. Often multiple regimes are needed to describe all radial positions, classes of particles, and helicities of the magnetic field for a single discharge. When collisions set the radial step size of trapped particles, the transport scales as $1/\nu$ where ν is the collision frequency. The $1/\nu$ regime can be relevant for both ripple trapped and banana particles. When the effective collision frequency is smaller than the toroidal drift frequency, fluxes from boundary layers become important. Transport from the collisional trapped-passing boundary layer leads to fluxes that scale as $\sqrt{\nu}$ and ν. When the collisionality is sufficiently low, the collisionless detrapping/retrapping layer becomes significant, where fluxes scale as ν. Banana particles can become passing particles due to the variation of B_{max} along their drift trajectory,[21] and ripple trapped particles can also experience collisionless detrapping from ripple wells to become toroidally trapped.[22,23] If the collisionality is small compared with the typical toroidal precession frequency of trapped particles, the resonant velocity space layer where the bounce-averaged toroidal drift vanishes can experience significant radial drifts, leading to superbanana-plateau transport.[24] In the presence of a strong radial electric field, the bounce-harmonic resonance between the parallel bounce motion and drift motion of trapped particles can also result in enhanced transport.[25,26] The $1/\nu$ and $\sqrt{\nu}$ stellarator regimes for helically-trapped particles have been formulated by Galeev and Sagdeev,[27] Ho and Kulsrud,[28] and Frieman.[29] These results were generalized to rippled tokamaks in the $1/\nu$ regime by Stringer[20] and Connor and Hastie[30] and in the $\sqrt{\nu}$ regime by Kovrizhnykh.[31] Linsker and Boozer[25] evaluated banana diffusion

particle and heat transport in the $1/\nu$ and ν regimes, and Davidson[32] evaluated banana diffusion $1/\nu$ transport. Shaing has formulated the theory for NTV torque due to banana diffusion in the $1/\nu$,[33] $\nu - \sqrt{\nu}$,[34] ν,[21] and superbanana-plateau[24] regimes in addition to an approximate analytic formula which connects these regimes.[35]

The calculation of NTV torque requires two steps: (i) determine the equilibrium magnetic field in the presence of ripple and (ii) solve a drift kinetic equation (DKE) with the magnetohydrodynamic (MHD) equilibrium or apply reduced analytic formulae. The first step can be performed using various levels of approximation. The simplest method is to superimpose 3D ripple vacuum fields on an axisymmetric equilibrium, ignoring the plasma response. A second level of approximation is to use a linearized 3D equilibrium code such as the Ideal Perturbed Equilibrium Code (IPEC)[26] or linear MD3-C1.[36] A third level of approximation is to solve nonlinear MHD force balance using a code such as the Variational Moments Equilibrium Code (VMEC)[37] or M3D-C1[38] run in nonlinear mode. In this paper we use free-boundary VMEC to find the MHD equilibrium in the presence of toroidal field ripple, FIs, and TBMs.

Many previous NTV calculations[6,13,26,39] have been performed using reduced analytic models, although a DKE must be solved numerically in order to avoid severe assumptions. Solutions of the bounce-averaged kinetic equation have been found to agree with Shaing's analytic theory except in the transition between regimes.[40] However, the bounce-averaged kinetic equation does not include contributions from bounce and transit resonances. Discrepancies have been found between numerical evaluation of NTV using the Monte Carlo neoclassical solver FORTEC-3D and analytic formulae for the $1/\nu$ and superbanana-plateau regimes.[41,42] The quasilinear NEO-2 has been found to differ from Shaing's connected formulae,[35] especially in the edge where the large aspect ratio assumption breaks down.[43] Rather than applying such reduced models, in this paper a DKE is solved using the Stellarator Fokker-Planck Iterative Neoclassical Conservative Solver (SFINCS)[44] to calculate neoclassical particle and heat fluxes for an ITER steady-state scenario. The SFINCS code does not exploit any expansions in collisionality, size of perturbing field, or magnitude of the radial electric filed. It also allows for realistic experimental magnetic geometry rather than using simplified flux surface shapes. All trapped particle effects including ripple-trapping,[20] banana diffusion,[25] and bounce-resonance[25] are accounted for in these calculations. The DKE solved by SFINCS en-

sures intrinsic ambipolarity for axisymmetric or quasisymmetric flux surfaces in the presence of a radial electric field while this property is not satisfied by other codes such as DKES.[45,46] This prevents spurious NTV torque density, which is proportional to the radial current. As SFINCS makes no assumption about the size of ripple, it can account for nonlinear transport due to locally trapped particles. The deviation from the quasilinear assumption has been found to be significant in benchmarks between SFINCS and NEO-2.[43]

In addition to NTV, neutral beams will provide an angular momentum source for ITER. As NBI torque scales as $P/E^{1/2}$ for input power P and particle energy E, ITER's neutral beams, with $E = 1$ MeV and $P = 33$ MW, will provide less momentum than in other tokamaks such as JET, with $E = 125$ keV for $P = 34$ MW.[47] NBI-driven rotation will also be smaller in ITER because of its relatively large moment of inertia, with major radius $R = 6$ m compared to 3 m for JET.

However, spontaneous rotation may be significant in ITER. Turbulence can drive significant flows in the absence of external momentum injection, known as intrinsic or spontaneous rotation. This can be understood as a turbulent redistribution of toroidal angular momentum to produce large directed flows. For perturbed tokamaks this must be in the approximate symmetry direction. According to gyrokinetic orderings and inter-machine comparisons by Parra,[48] intrinsic toroidal rotation scales as $V_\zeta \sim T_i/I_p$ where T_i is the ion temperature and I_p is the plasma current, and core rotations may be on the order of 100 km/s (ion sonic Mach number $M_i \approx 8\%$) in ITER. Scalings with $\beta_N = \beta_T a B_T/I_P$, where $\beta_T = 2\mu_0 P/B_T^2$, B_T is the toroidal magnetic field in tesla, a is the minor radius in meters, and P is the plasma pressure, by Rice[49] predict rotations of a similar scale, $M_i \approx 30\%$ or $V_\zeta \approx 400$ km/s. Co-current toroidal rotation appears to be a common feature of H-mode plasmas and has been observed in electron cyclotron heated (ECH),[50] ohmic,[50] and ion cyclotron range of frequencies (ICRF)[51] heated plasmas. Gyrokinetic GS2 simulations have also shown that low collisionality tokamaks have an inward radial momentum flux, corresponding to a rotation profile peaked in the core toward the co-current direction.[52] In an up-down symmetric tokamak, radial intrinsic angular momentum flux can be shown to vanish to lowest order in $\rho_* = \rho_i/a$, where $\rho_i = v_{ti} m_i c/eB$ is the gyroradius and $v_{ti} = \sqrt{2T_i/m_i}$ is the ion thermal velocity, but neoclassical departures from an equilibrium Maxwellian can break this symmetry and cause non-zero rotation in the absence of input momentum.[52]

In section II the ITER steady state scenario considered is discussed. In section III free boundary MHD equilibrium in the presence of field ripple are presented. In section IV we estimate rotation driven by NBI and turbulence. This flow velocity is related to E_r in section V. The influence of TF ripple, TBMs, and FIs on neoclassical transport is evaluated, and a radial profile of torque is presented in section VI. In section VII the scaling of transport calculated with SFINCS is compared with that predicted by NTV theory, and in section VIII neoclassical heat fluxes in the presence of ripple are presented. In section IX, we assess several tangential magnetic drift models on the transport for this ITER scenario. In section X we summarize the results and conclude.
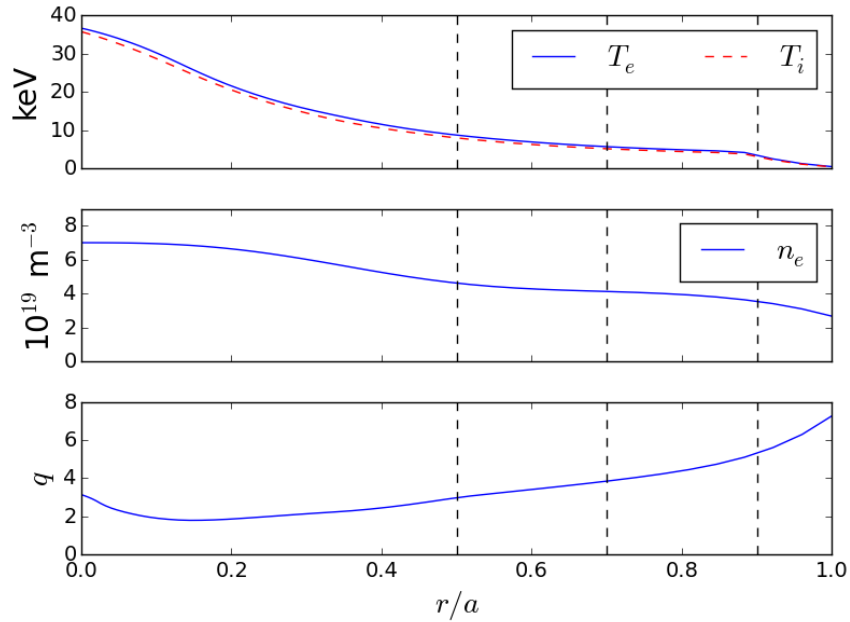
II.   ITER STEADY STATE SCENARIO

FIG. II.1.   Radial profiles of temperature, density, and safety factor for the ITER steady state scenario.[53] Black dashed lines indicate the radial locations that will be considered for neoclassical calculations.

We consider an advanced ITER steady state scenario with significant bootstrap current and reversed magnetic shear.[53] The input power includes 33 MW NBI, 20 MW electron cyclotron (EC), and 20 MW lower hybrid (LH) heating for a fusion gain of $Q = 5$ and toroidal

current of 9 MA. The discharge was simulated using the Tokamak Simulation Code (TSC)[54] and TRANSP[55] using a Coppi-Tang[56] transport model and EPED1[57] pedestal modeling. The density, temperature, and safety factor q profiles are shown in figure II.1. For neoclassical calculations we consider a three species plasma (D, T, and electrons), and we assume that $n_D = n_T = n_e/2$. Neoclassical transport will be analyzed in detail at the radial locations indicated by dashed horizontal lines ($r/a = 0.5, 0.7, 0.9$). Throughout we will use the radial coordinate $r/a \propto \sqrt{\Psi_\mathrm{T}}$ where Ψ_T is the toroidal flux.

III. FREE BOUNDARY EQUILIBRIUM CALCULATIONS AND RIPPLE MAGNITUDE

The magnetic equilibrium was computed using the density, temperature, and q profiles from TRANSP along with filamentary models of the toroidal field (TF), poloidal field (PF), and center stack (CS) coils and their corresponding currents. The vacuum fields produced by the three TBMs and the FIs have been modeled using FEMAG.[58] The VMEC free-boundary equilibrium[37] is computed for four geometries: (i) including only the TF ripple, (ii) including TF ripple, TBMs, and FIs, (iii) TF ripple and FIs, and (iv) axisymmetric geometry.

We define the magnitude of the magnetic field ripple to be,

$$\delta_B = (B_\mathrm{max} - B_\mathrm{min})/(B_\mathrm{max} + B_\mathrm{min}), \qquad (\mathrm{III}.1)$$

where the maximum and minimum are evaluated at fixed radius and poloidal angle θ. In figure III.1, δ_B is plotted on the poloidal plane for the three rippled VMEC equilibria. A fourth case is also shown in which the component of $\boldsymbol{B}$ with $|n| = 18$ was removed from the geometry with TBMs and FIs in order to demonstrate the magnitude of the ripple produced by the TBMs alone (bottom right). When only TF ripple is present, significant ripple persists over the entire outboard side, while in the configurations with FIs the ripple is much more localized in θ. When TBMs are present, the ripple is higher in magnitude near the outboard midplane ($\delta_B \approx 1.4\%$), while in the other magnetic configurations $\delta_B \approx 1\%$ near the outboard midplane. For comparison, the TF ripple during standard operations is 0.08% in JET[8] and 0.6% in ASDEX Upgrade.[43]

In figure III.2, the magnitude of $\boldsymbol{B}$ is plotted as a function of toroidal angle ζ at $\theta = 0$ and $\theta = \pi/4$. Away from the midplane ($\theta = \pi/4$) the FIs greatly decrease the magnitude of the

TF ripple. Near the midplane the FIs do not decrease the magnitude of the toroidal ripple as strongly, as the number of steel plates is reduced near the midplane.[58] The ferromagnetic steel of the TBMs concentrates magnetic flux and locally decreases B in the plasma near its location. This adds an enhancement of δ_B near $\theta = 0$.
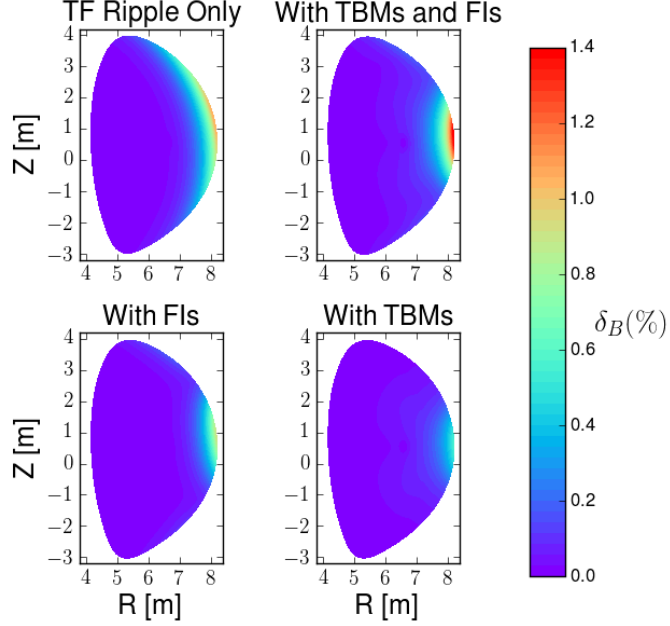

FIG. III.1. Magnetic field ripple, $\delta_B = (B_{\mathrm{max}} - B_{\mathrm{min}})/(B_{\mathrm{max}} + B_{\mathrm{min}})$, is plotted on the poloidal plane for VMEC free boundary equilibria including (i) only TF ripple (top left), (ii) TF ripple, TBMs, and FIs (top right), (iii) TF ripple and FIs (bottom left), and (iv) with TBMs only (bottom right). FIs decrease the poloidal extent of the ripple, while TBMs add an additional ripple near the outboard midplane.
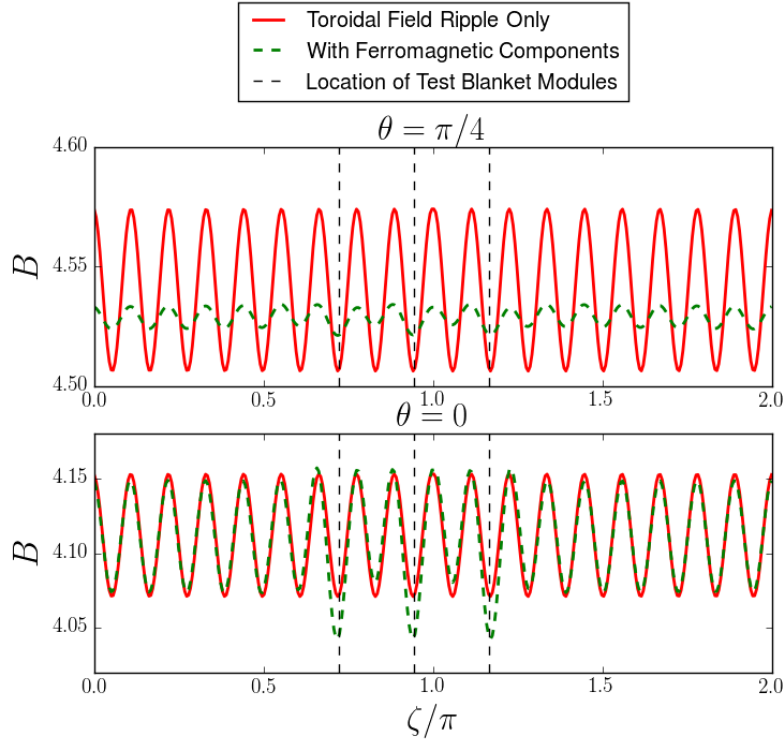
FIG. III.2. The magnitude of $\boldsymbol{B}$ as a function of toroidal angle (ζ) at $r/a = 1$, $\theta = 0$ and $\pi/4$. Vertical dashed lines indicate the toroidal locations of the TBM ports. The mitigating effect of the FIs is stronger away from the midplane, where an increased number of steel plates are inserted. The TBMs add an additional ripple near their locations at $\theta = 0$.

IV. ESTIMATING TOROIDAL ROTATION

In order to predict the ripple transport in ITER, the radial electric field, $E_r = -\Phi'(r)$, must be estimated, as particle and heat fluxes are nonlinear functions of E_r. This is equivalent to predicting the parallel flow velocity, $V_{||}$, which scales monotonically with E_r. As we simply wish to determine a plausible value of E_r, the difference between $V_{||}$ and $V_\zeta = \Omega_\zeta(r)\langle R \rangle$, the toroidal flow, will be unimportant for our estimates. Here the flux surface average is denoted by $\langle ... \rangle$,

$$\langle ... \rangle = \frac{1}{V'} \int_0^{2\pi} d\theta \int_0^{2\pi} d\zeta \sqrt{g}(...) \tag{IV.1}$$

$$V' = \int_0^{2\pi} d\theta \int_0^{2\pi} d\zeta \sqrt{g}, \tag{IV.2}$$

10

where $\sqrt{g}$ is the Jacobian. As B and I_P will be parallel in ITER, V_ζ and $V_\parallel$ point in the same direction. In our calculation of V_ζ the neoclassical torque is ignored. Instead E_r is viewed as an input to neoclassical calculations from which the NTV torque can be obtained. For this rotation calculation, angular momentum transport due to neutral beams and turbulence will be considered. There is an additional torque caused by the radial current of orbit-lost alphas,[59] but it will be negligible (≈ 0.006 Nm/m^3). The following time-independent momentum balance equation is considered in determining $\Omega_\zeta(r)$,

$$\nabla \cdot \Pi_\zeta^{\text{turb}}(\Omega_\zeta) + \nabla \cdot \Pi_\zeta^{\text{NC}}(\Omega_\zeta) = \tau^{\text{NBI}}, \tag{IV.3}$$

where Π_ζ^{turb} and Π_ζ^{NC} are the toroidal angular momentum flux densities due to turbulent and neoclassical transport and τ^{NBI} is the NBI torque density. For this paper the feedback of Π_ζ^{NC} on Ω_ζ will not be calculated. Determining the change in rotation due to NTV would require iteratively solving this equation for Ω_ζ, as Π_ζ^{NC} is a nonlinear functions of Ω_ζ.

The quantity Π_ζ^{turb} consists of a diffusive term as well as a term independent of Ω_ζ which accounts for turbulent intrinsic rotation. An angular momentum pinch will not be considered for this analysis.

$$\Pi_\zeta^{\text{turb}} = -m_i n_i \chi_\zeta \langle R^2 \rangle \frac{\partial \Omega_\zeta}{\partial r} + \Pi_{\text{int}} \tag{IV.4}$$

Here m_i is the ion mass, n_i is the ion density, and χ_ζ is the toroidal ion angular momentum diffusivity. Ignoring NTV torque, we will solve the following angular momentum balance equation,

$$m_i \frac{1}{V'} \frac{\partial}{\partial r} \left(V' n_i \chi_\zeta \langle R^2 \rangle \frac{\partial \Omega_\zeta}{\partial r} \right) = -\frac{1}{V'} \frac{\partial}{\partial r} \left(V' \Pi_{\text{int}} \right) + \tau^{\text{NBI}}. \tag{IV.5}$$

Eq. IV.5 is is a linear inhomogeneous equation for Ω_ζ, as the right hand side is independent of Ω_ζ. We can therefore solve for the rotation due to each of the source terms individually and add the results to obtain the rotation due to both NBI torque and turbulent intrinsic torque.

The NBI-driven rotation profile is evolved by TRANSP assuming $\chi_\zeta = \chi_i$, the ion heat diffusivity. The total beam torque density, τ^{NBI}, is calculated by NUBEAM including collisional, $\boldsymbol{J} \times \boldsymbol{B}$, thermalization, and recombination torques. The following momentum balance equation is solved to compute Ω_ζ driven by NBI,

$$\tau^{\text{NBI}} = -\frac{1}{V'} \frac{\partial}{\partial r} \left(V' m_i n_i \chi_i \langle R^2 \rangle \frac{\partial \Omega_\zeta}{\partial r} \right). \tag{IV.6}$$

We consider a semi-analytic intrinsic rotation model to determine the turbulent-driven rotation,[60]

$$\Omega_\zeta(r) = -\int_r^a \frac{v_{ti}\rho_{*,\theta}}{2P_r L_T^2}\widetilde{\Pi}(\nu_*)\,dr', \qquad (IV.7)$$

where $\rho_{*,\theta} = v_{ti}m_i/(eB_\theta\langle R\rangle)$ is the poloidal normalized gyroradius, and the Prandtl number $P_r = \chi_\zeta/\chi_i$ is taken to be 1. The normalized collision frequency is $\nu_* = qRv_{ti}/(\nu_{ii}\epsilon^{3/2})$ where $\epsilon = r/\langle R\rangle$ is the inverse aspect ratio and $L_T = -\left(\partial\ln T_i/\partial r\right)^{-1}$ is the temperature gradient scale length. Equation IV.7 is obtained assuming that Π_{int} balances turbulent momentum diffusion in steady state, $\Pi_{int} = m_i n_i \chi_\zeta\langle R^2\rangle\partial\Omega_\zeta/\partial r$. This model considers the intrinsic torque driven by the neoclassical diamagnetic flows, such that $\Omega_\zeta \sim \rho_{*,\theta}v_{ti}/\langle R\rangle$ and $\Omega_\zeta\Pi_{int}/Q \sim \rho_{*,\theta}$. It is also assumed that $\Omega_\zeta = 0$ at the wall.

The quantity $\widetilde{\Pi}(\nu_*)$ is an order unity function which characterizes the collisionality dependence of rotation reversals, determined from gyrokinetic turbulence simulations,[52]

$$\widetilde{\Pi}(\nu_*) = \frac{(\nu_*/\nu_c - 1)}{1 + (\nu_*/\nu_c)}, \qquad (IV.8)$$

where $\nu_c = 1.7$. Because of ITER's low collisionality, we do not expect a rotation reversal, which is correlated with transitioning between the banana and plateau regimes. Equation IV.7 was integrated using profiles for the ITER steady state scenario.

The rotation predicted by these models is shown in figure IV.1. NBI torque contributes to significant rotation at $r/a \lesssim 0.4$ where the torque density also peaks (see figure VI.5), while turbulent torque produces rotation in the pedestal due to the L_T^{-2} scaling of our model. The intrinsic rotation calculated is comparable to that predicted from theoretical scaling arguments by Parra,[48] $V_\zeta \approx 100$ km/s. At the radii that will be considered for neoclassical calculations (indicated by dashed vertical lines), intrinsic turbulent rotation may dominate over that due to NBI. However, we emphasize that is is an estimate based on scaling arguments, as much uncertainty is inherent in predicting turbulent rotation.

For stabilization of the resistive wall mode (RWM) in ITER, it has been estimated that a critical central rotation frequency $\Omega_\zeta(0) \gtrsim 5\%$ of the Alfvèn frequency, $\omega_A = B/(\langle R\rangle\sqrt{\mu_0\rho_i})$, must be achieved given a peaked rotation profile.[5] With a central rotation of $\Omega_\zeta(0) \approx 2\%\,\omega_A$ in figure IV.1, it may be difficult to suppress the RWM in ITER with rotation alone. As this calculation does not take into account magnetic braking, $\Omega_\zeta(0)/\omega_A$ is likely to be smaller than
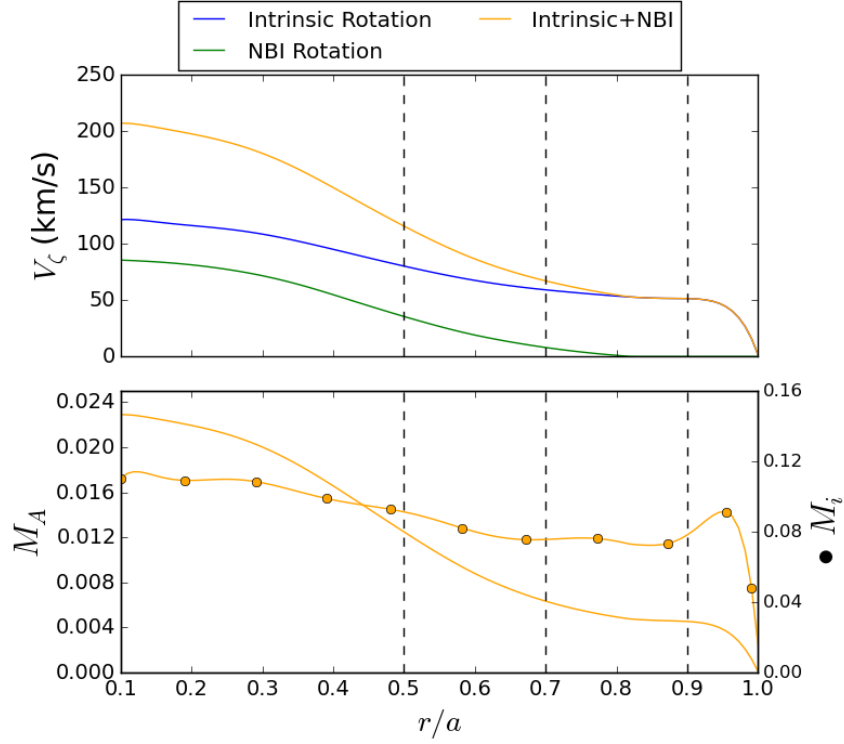
FIG. IV.1. Toroidal rotation V_ζ due to turbulence and NBI (top) is shown along with corresponding Alfvèn Mach number (bottom, solid), and ion sonic Mach number (bottom, bulleted). The intrinsic rotation calculation uses a semi-analytic model of turbulent momentum redistribution.[60] The NBI rotation is calculated from turbulent diffusion of NBI torque using NUBEAM and TRANSP.[53] Dashed vertical lines indicate the radial positions where SFINCS calculations are performed.

what is shown. Additionally, the TBM are known to increase the critical rotation frequency as they have a much shorter resistive time scale than the wall.[5] More recent analysis has shown that even above such a critical rotation value, the plasma can become unstable due to resonances between the drift frequency and bounce frequency.[61,62]

V. RELATIONSHIP BETWEEN E_r AND $V_{||}$

Neoclassical theory predicts a specific linear-plus-offset relationship between $V_{||}$ and E_r, but it does not predict a particular value for either $V_{||}$ or E_r in the presence of symmetry-breaking. Neoclassical calculations of $V_{||}$ are made in order to determine an E_r profile

consistent with the our estimate of $V_\zeta \approx \langle V_{||} B \rangle / \langle B^2 \rangle^{1/2}$ made in section IV. The parallel flow velocity for species a is computed from the neoclassical distribution function,

$$V_{||}^a = \left(\frac{1}{n_a} \right) \int d^3 v \, v_{||} f_a, \qquad \text{(V.1)}$$

which we calculate with the SFINCS[44] code.

SFINCS is used to solve a radially-local DKE for the gyro-averaged distribution function, f_{a1}, on a single flux surface including coupling between species.

$$(v_{||} \boldsymbol{b} + \boldsymbol{v}_E + \boldsymbol{v}_{ma}) \cdot (\nabla f_{a1}) - C(f_{a1}) = -\boldsymbol{v}_{ma} \cdot \nabla \psi \left(\frac{\partial f_{a0}}{\partial \psi} \right) + \frac{Z_a e v_{||} B \langle E_{||} B \rangle}{T_a \langle B^2 \rangle} f_{a0} \qquad \text{(V.2)}$$

Here a indicates species, f_{a0} is an equilibrium Maxwellian, $\psi = \Psi_\mathrm{T}/2\pi$, and C is the linearized Fokker-Planck collision operator. Gradients are performed at constant $W = m_a v^2/2 + Z_a e \Phi$ and $\mu = v_\perp^2/(2B)$. The $\boldsymbol{E} \times \boldsymbol{B}$ drift is

$$\boldsymbol{v}_E = \frac{1}{B^2} \boldsymbol{B} \times \nabla \Phi \qquad \text{(V.3)}$$

and the radial magnetic drift is

$$\boldsymbol{v}_{ma} \cdot \nabla \psi = \frac{1}{2\Omega_a B} \left(v_{||}^2 + \frac{v_\perp^2}{2} \right) \boldsymbol{b} \times \nabla B \cdot \nabla \psi, \qquad \text{(V.4)}$$

where $v_\perp$ is the velocity coordinate perpendicular to $\boldsymbol{b}$. The quantity $\Omega_a = Z_a e B / m_a$ is the gyrofrequency. Transport quantities have been calculated using the steady state scenario ion and electron profiles and VMEC geometry. The second term on the right hand side of eq. V.2 proportional to $E_{||}$ is negligible for this non-inductive scenario with loop voltage $\approx 10^{-4}$ V. For the calculations presented sections V, VI, VII, and VIII, $\boldsymbol{v}_{ma} \cdot \nabla f_{a1}$ is not included. The effect of keeping this term is shown to be small in section IX.

The relationship between E_r and $\langle V_{||} B \rangle / \langle B^2 \rangle^{1/2}$ for electrons and ions at $r/a = 0.9$ is shown in figure V.1. Note that only one curve is shown for each species as the addition of ripple fields did not change the dependence of $V_{||}$ on E_r significantly ($\leq 5\%$). While radial transport of heat and particles changes significantly in the presence of small ripple fields (see sections VI, VII, and VIII), the parallel flow is much less sensitive to the perturbing field. It can be shown (see appendix A) that when axisymmetry is broken the component of f_1 that contributes to $V_{||}$ is of higher order in $\nu_* \ll 1$ than the component that contributes to the radial particle fluxes, Γ_ψ, and NTV torque density.
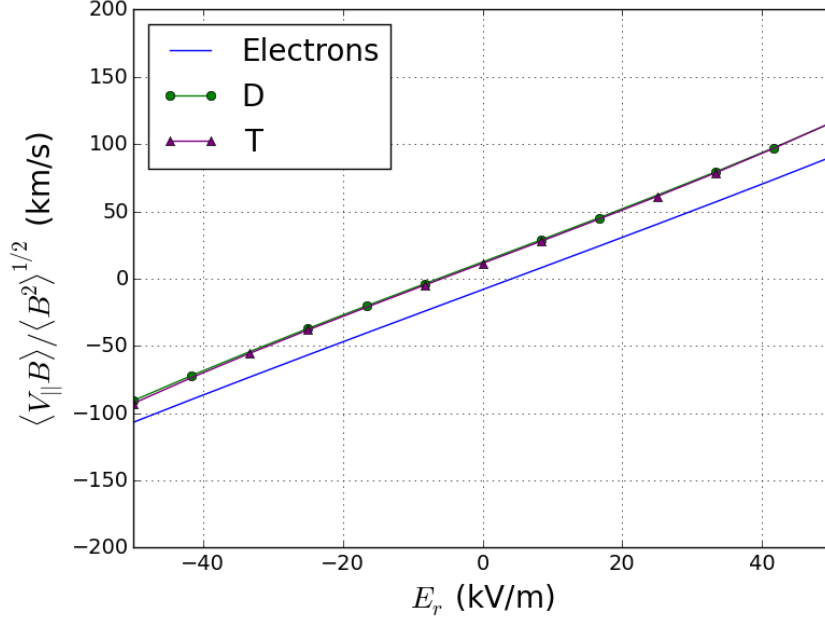
14

FIG. V.1.   SFINCS calculation of the flux surface averaged parallel flow, $\langle BV_{||}\rangle/\langle B^2\rangle^{1/2}$, at $r/a = 0.9$ for ions and electrons. The addition of ripple does not change the tokamak neoclassical relationship between E_r and $V_{||}$ by a discernible amount on this scale although the radial particle fluxes, Γ_ψ, are sensitive to the perturbing field.

We can write $\langle BV_{||}^a\rangle$ in terms of dimensionless transport coefficients L_{31} and L_{32} and thermodynamic drives,

$$\langle V_{||}^a B\rangle = L_{31}\frac{cG}{Z_a e n_a}\left[\frac{1}{n}\frac{d(nT)}{d\psi_P} + Z_a e\frac{d\Phi}{d\psi_P} + k_{||}\frac{cG}{Z_a e n_a}\frac{dT}{d\psi_P}\right], \qquad (V.5)$$

where $2\pi\psi_P$ is the poloidal flux, G is defined through $\boldsymbol{B} = \beta\nabla\psi + I(\psi)\nabla\theta + G(\psi)\nabla\zeta$ for Boozer angles θ and ζ, and $k_{||} = (L_{32}/L_{31} - 5/2)$ is the parallel flow coefficient. The low collisionality, large aspect ratio limit[63,64] $k_{||} \approx 1.17$ is often assumed in NTV theory[65,66] in relating analytic expressions of torque density to toroidal rotation frequency. The value of $k_{||}$ calculated by SFINCS for ITER parameters varies between 1.6 near the edge and 0.6 near the core.

VI. TORQUE CALCULATION

The NTV torque density, τ^{NTV}, is calculated from radial particle fluxes, Γ_ψ,

$$\Gamma_{\psi,a} = \left\langle \int d^3v (\boldsymbol{v}_{\mathrm{m}a} \cdot \nabla\psi) f_a \right\rangle, \qquad (\mathrm{VI.1})$$

using the flux-friction relation,

$$\tau^{\mathrm{NTV}} = -B^\theta \sum_a n_a q_a \Gamma_{\psi,a}, \qquad (\mathrm{VI.2})$$

where $B^\theta = \boldsymbol{B} \cdot \nabla\theta$ and the summation is performed over species. This expression relates radial particle transport to a toroidal angular momentum source caused by the non-axisymmetric field. This relationship can be derived from action-angle coordinates,[67] neoclassical moment equations,[68] or from the definition of the drift-driven flux.[69]

The calculation of τ^{NTV} for three geometries at $r/a = 0.9$ is shown in figure VI.1. Here positive corresponds to the co-current direction. The numerically computed NTV torque is found to vanish in axisymmetric geometry, as expected. Overall, the magnitude of τ^{NTV} with only TF ripple is larger than that with the addition of both the FIs and the TBMs. In figure VI.3 we show that the $|n| < 18$ TBM ripple produces much less torque than the $|n| = 18$ component of B, so the decrease in τ^{NTV} magnitude with both FIs and TBMs can be attributed to the decrease in ripple in the presence of FIs. As will be discussed in section VII, neoclassical ripple transport in most regimes scales positively with δ_B. The addition of FIs significantly decreases the magnitude of δ_B across most of the outboard side, and as a result the magnitude of τ^{NTV} is significantly decreased. The dashed vertical line indicates the value of $\langle V_\| B \rangle / \langle B^2 \rangle^{1/2}$ and E_r predicted from the intrinsic and NBI rotation model. At this value of E_r the presence of ferritic components decreases the magnitude of the torque density by about 75%.

The circle indicates the offset rotation at the ambipolar E_r. If no other angular momentum source were present in the system, τ^{NTV} would drive the plasma to rotate at this velocity. Although τ^{NTV} differs significantly between the two geometries they have similar offset rotation velocities, $V_\zeta = $ -10 km/s with TF ripple only and -6 km/s with TBMs and FIs. Note that for E_r greater than this ambipolar value, τ^{NTV} is counter-current while neutral beams and turbulence drive rotation in the co-current direction, so τ^{NTV} is a damping

16

torque. The NTV torque due to TF ripple only is larger in magnitude than τ^{NBI} while that with TBMs and FIs is of similar magnitude (see figure VI.5). NTV may also compete with the turbulent torque, $\tau^{\mathrm{turb}} = -\nabla \cdot \Pi_{\mathrm{int}} \approx 0.05$ Nm/m^3 at this radius. Therefore, NTV torque may be key in determining the edge rotation in ITER.

Note that the magnitude of τ^{NTV} peaks near $E_r = 0$ where $1/\nu$ transport becomes dominant. Although ν_* is sufficiently small such that the superbanana-plateau regime may be significant, the physics of superbanana formation is not included in these SFINCS calculations which do not include $\boldsymbol{v}_{\mathrm{m}} \cdot \nabla f_1$. Superbanana-plateau transport will be considered in section IX. While the $1/\nu$ regime is avoided due to the sufficiently large $|E_r|$ estimate at this radius, $1/\nu$ transport may become significant at smaller radii, as will be discussed below. The peak at small $|E_r|$ also corresponds to the region where $1/\nu$ transport of particles trapped in local ripple wells becomes relevant. Because of ITER's low collisionality, $\nu_* \ll (\delta/\epsilon)^{3/4}$, diffusion due to ripple trapping may compete with banana diffusion.[70] We have confirmed that the TF ripple causes local wells along the field line, corresponding to $\alpha = \epsilon/(qN\delta_B) < 1$.[20] Much NTV literature is based on banana diffusion and ripple trapping in the $1/\nu$ regime,[20,71] which is not applicable for the range of E_r applicable to ITER. At $r/a = 0.9$, the $1/\nu$ regime applies for $|E_r| \lesssim 0.2$ kV/m where the effective collision frequency of trapped particles is larger than the $E \times B$ precession frequency.

NTV torque is often expressed in terms of a toroidal damping frequency, ν_ζ,

$$\tau^{\mathrm{NTV}} = -\nu_\zeta \langle R^2 \rangle mn(\Omega_\zeta - \Omega_{\zeta,\mathrm{offset}}), \tag{VI.3}$$

where $\Omega_{\zeta,\mathrm{offset}}$ is the offset rotation frequency. We note that τ^{NTV} does appear to scale linearly with E_r (and thus Ω_ζ) for $|E_r| \gtrsim 30$ kV/m. However, τ^{NTV} is a complicated nonlinear function of Ω_ζ for $|E_r| \lesssim 30$ kV/m at the transition between collision-limited superbanana-plateau transport and $\sqrt{\nu} - \nu$ transport.

In figure VI.2 we present the contribution to the NTV torque (τ^{NTV}) density at $r/a = 0.9$ by the electrons and ions in the presence of TF ripple only (left) and TF ripple with ferromagnetic components (right). Note that the E_r corresponding to the offset rotation frequency for the electrons is positive while that of the ions is negative. At the E_r predicted by the intrinsic and NBI rotation model, τ^{NTV} due to the electron particle flux is positive while that due to ion particle flux is negative. At all radial locations the electron contribution
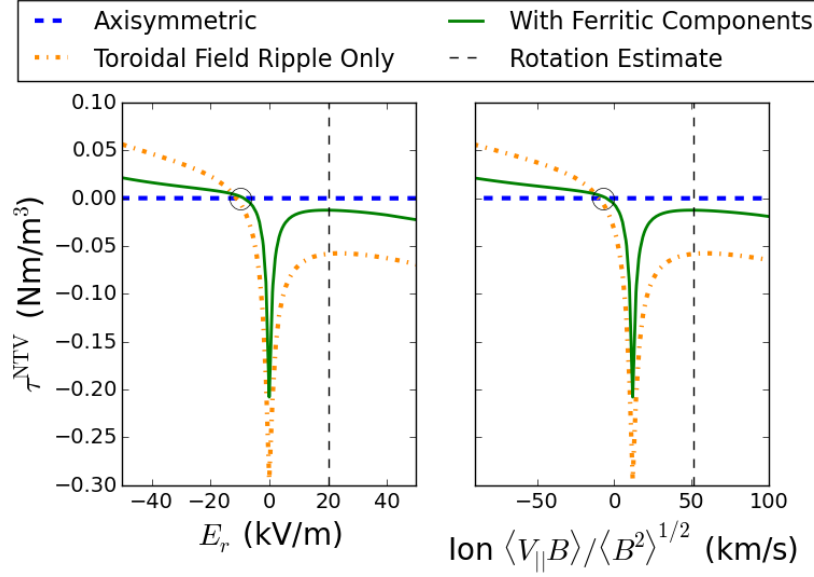
FIG. VI.1. SFINCS calculation of NTV torque density as a function of E_r and ion $\langle V_{||}B\rangle/\langle B^2\rangle^{1/2}$ at $r/a = 0.9$ is shown for 3 VMEC geometries: (i) axisymmetric (blue dashed), (ii) with TF ripple only (orange dash-dot), and (iii) TF ripple with FIs and TBMs (green solid). The vertical dashed line indicates the estimate of E_r and $V_\zeta \approx \langle V_{||}B\rangle/\langle B^2\rangle^{1/2}$ based on the intrinsic and NBI rotation model. The circle denotes the offset rotation at $V_{||} \approx -10$ km/s. The magnitude of τ^{NTV} at this radius is of similar magnitude to the NBI and turbulent torques but is opposite in direction (see figure VI.5).

to τ^{NTV} is less than 10% of the total torque density.

In order to decouple the influence of the FI ripple and the TBM ripple, τ^{NTV} at $r/a = 0.9$ is calculated for toroidal modes (i) $|n| \le 18$, (ii) $|n| = 18$, and (iii) $|n| < 18$, shown in figure VI.3. For $|n| \le 18$ and $|n| = 18$, VMEC free boundary equilibria were computed including these toroidal modes. For $|n| < 18$, the SFINCS calculation was performed to include the desired n from the VMEC fields. Here B was decomposed as,

$$B = \sum_{m,n} b_{mnc}\cos(m\theta - n\zeta) + b_{mns}\sin(m\theta - n\zeta), \qquad (VI.4)$$

where θ and ζ are VMEC angles. The quantities $B^{\theta,\zeta}, B_{r,\theta,\zeta}, \sqrt{g}$, and position vectors $\dfrac{\partial \boldsymbol{r}}{\partial x^k}$ and ∇x^k are similarly decomposed such that the DKE can be solved for the desired toroidal
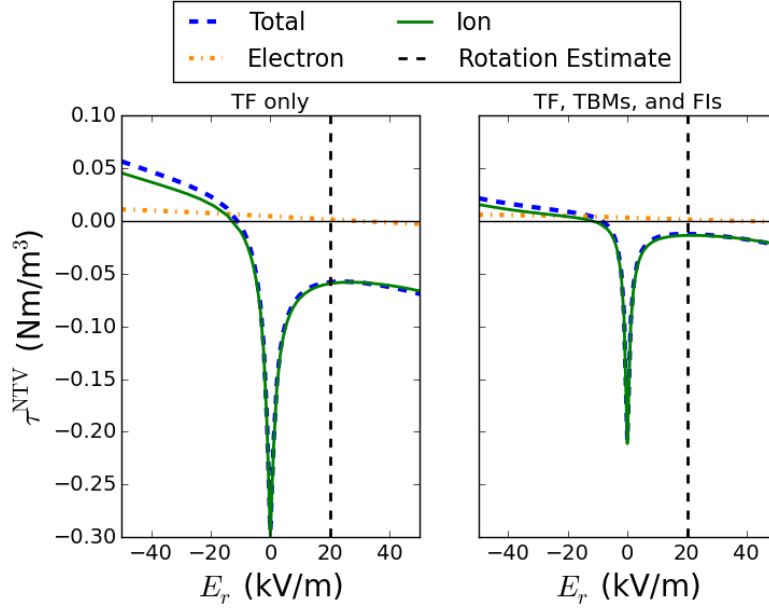
18

FIG. VI.2. Total (blue dashed), electron (yellow dash-dot), and ion (green solid) contributions to NTV torque density at $r/a = 0.9$ for TF ripple only geometry (left) and TF ripple with ferromagnetic components (right). The dashed vertical line indicates the E_r predicted by the intrinsic and NBI rotation model. The electrons have a co-current neoclassical offset rotation and contribute a small co-current NTV torque density at the E_r predicted by the rotation model.

modes.

We note that although the TBM ripple is largely an $|n| = 1$ perturbation, there is a small contribution to the $|n| = 18$ ripple. While the FIs decrease the magnitude of the $|n| = 18$ component of B, the TBM contributes most strongly to low mode numbers. As SFINCS is not linearized in the perturbing field, the torque due to both FIs and TBMs is not the sum of the torques due to these ripple fields considered individually.

We find that the $|n| = 18$ component drives about 100 times more torque than the other components of B. This result is in a agreement with most relevant rippled tokamak transport regimes feature positive scaling with n. For tokamak banana diffusion in the $\sqrt{\nu}$ regime[34] ion transport scales as $\Gamma_\psi \sim \sqrt{n}$ and in the $1/\nu$ regime[33] $\Gamma_\psi \sim n^2$. In the collisionless detrapping-retrapping ripple transport regime,[22,23] $\Gamma_\psi \propto G(\alpha)$ where $G(\alpha)$ increases with increasing n. Moreover, the low mode number ripple does not result in local ripple wells along a field line.

This matches our findings that the higher harmonic $|n| = 18$ ripple contributes more strongly to τ^{NTV} than the $|n| < 18$ ripple.
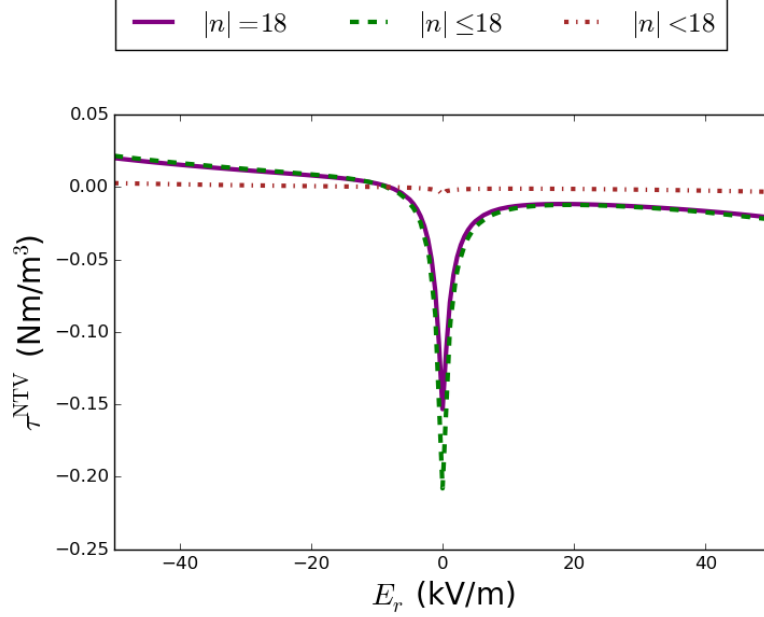

FIG. VI.3. The NTV torque density at $r/a = 0.9$ for toroidal mode numbers (i) $|n| = 18$ (purple solid), (ii) $|n| < 18$ (brown dash dot), and (iii) $|n| \leq 18$ (green dashed). The TBM ripple contributes most strongly to low $|n|$, while the FIs and TF ripple contribute to $|n| = 18$. The low n TBM ripple does not contribute as strongly to the NTV torque density as the $|n| = 18$ component of $\boldsymbol{B}$ does.

In figure VI.4, the SFINCS calculation of τ^{NTV} with TF ripple only is shown at $r/a = 0.5$, 0.7, and 0.9. For these three radii the maximum $\delta_B = 0.26\%$, 0.51%, and 0.82% respectively. As τ^{NTV} scales with δ_B in most rippled tokamak regimes, it is reasonable to expect that the magnitude of τ^{NTV} would decrease with decreasing radius. On the other hand, transport scales strongly with T_i. In the $\sqrt{\nu}$ banana diffusion regime[34] $\Gamma_\psi \sim v_{ti}^4 \sqrt{\nu_{ii}} \sim T_i^{5/4}$. The combined effect of decreased ripple and increased temperature with decreasing radius leads to comparable torques with decreasing radius in the presence of significant E_r. The scaling with T_i is even stronger in the $1/\nu$ banana diffusion regime[24], where $\Gamma_\psi \sim v_{ti}^4/\nu_i i \sim T_i^{7/2}$. Indeed, we find that the magnitude of τ^{NTV} at $E_r = 0$ increases with decreasing radius.

In figure VI.5, we compare the magnitude of τ^{NTV} with τ^{NBI} and $\tau^{\mathrm{turb}} = -\nabla \cdot \Pi_{\mathrm{int}}$, the turbulent momentum source causing intrinsic rotation. For the τ^{NTV} profile, the in-
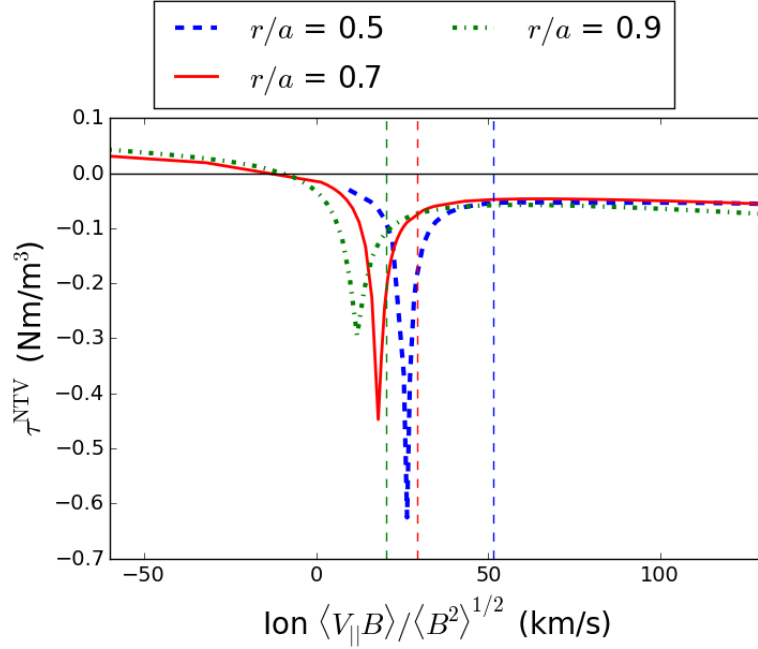
FIG. VI.4. SFINCS calculation of NTV torque density (τ^{NTV}) as a function of ion $\langle V_{\|}B\rangle/\langle B^2\rangle^{1/2}$ for VMEC geometry with TF ripple only at $r/a = 0.5$ (blue solid), 0.7 (red dashed), and 0.9 (green dash-dot). Although the field ripple decreases with radius (maximum $\delta_B = 0.82\%$ at $r/a = 0.9$, $\delta_B = 0.51\%$ at $r/a = 0.7$, $\delta_B = 0.26\%$ at $r/a = 0.5$), transport near $E_r = 0$ increases with decreasing radius because of scaling of ripple transport with T_i.[33]

trinsic rotation model and NBI rotation model are used to estimate E_r at each radius. The quantity τ^{NBI} is determined from NUBEAM calculations,[53] and τ^{turb} is estimated using $\Pi_{\mathrm{int}} \sim (\rho_\theta/L_T)\widetilde{\Pi}(\nu_*)Q(\langle R\rangle/v_{ti})$ (see appendix B). At $r/a = 0.55$, τ^{NTV} with the NBI rotation model ($E_r = 0.03$ kV/m) is about 20 times larger than τ^{NTV} with the intrinsic rotation model ($E_r = 46.9$ kV/m), as the E_r predicted by the NBI model is small enough that $1/\nu$ transport may dominate. Note that the turbulent torque produces much rotation in the pedestal according to this model as $\tau^{\mathrm{turb}} \propto 1/L_T$. The integrated NTV torque with the turbulent rotation model, -40 Nm, is comparable to the NBI torque, 35 Nm, while the turbulent torque is significantly larger, 93 Nm. The integrated NTV torque with the NBI rotation model is -52 Nm.

In the region $0.5 \lesssim r/a \lesssim 0.9$, NTV torque may dominate the rotation profile and will likely significantly damp rotation, decreasing MHD stability. However, the resulting

rotation profile may be sheared because of the significant counter-current NTV source at the edge and co-current NBI source in the core. This may provide a rotation shear as high as $\Delta V_\zeta/\Delta r \approx 0.8(v_{ti}/R)$ near $r/a = 0.5$, possibly large enough to suppress microturbulence[72] and promote the formation of an internal transport barrier. The rotation shear may be even more significant if the rotation profile is similar to that predicted by the NBI rotation model because of the magnified τ^{NTV} near $r/a = 0.55$ where $E_r \approx 0$.
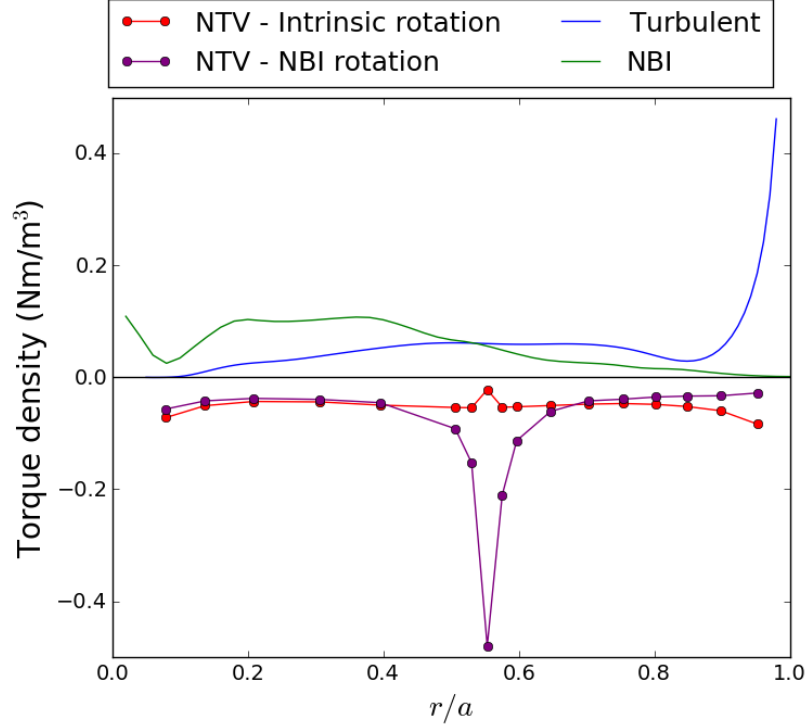

FIG. VI.5. Profiles of NTV torque density (τ^{NTV}) calculated with SFINCS, NBI torque density calculated from NUBEAM (τ^{NBI}), and estimate of turbulent intrinsic rotation momentum source (τ^{turb}). The quantity τ^{NTV} is calculated using E_r determined by the intrinsic rotation model and NBI rotation model described in section IV. Turbulent torque is estimated using $\tau^{\mathrm{turb}} \sim -\Pi_{\mathrm{int}}/a$ where $\Pi_{\mathrm{int}} \sim \rho_{*,\theta} \widetilde{\Pi}(\nu_*) Q \langle R \rangle / v_{ti}$ (see appendix B for details).

VII. SCALING WITH RIPPLE MAGNITUDE

The scaling of NTV transport with the magnitude of δ_B shows some agreement with that predicted by Shaing for the $\sqrt{\nu}$ and ν regimes.[21,34] In figure VII.1, the NTV torque density

calculated by SFINCS is shown as a function of the magnitude of the ripple, δ_B, for TF only geometry. The additional ferromagnetic ripple is not included, while the $|n| = 18$ components of $\boldsymbol{B}$, $\sqrt{g}$, and unit vectors are rescaled as described above. The quantity τ^{NTV} is calculated at $r/a = 0.9$ with $E_r = 30$ kV/m, corresponding to the intrinsic rotation estimate. The color-shaded background indicates the approximate regions of applicability of the $\sqrt{\nu}$ and ν banana diffusion regimes. The $1/\nu$ regime[33] does not apply at this E_r, as $\omega_E \gg \nu/\epsilon$ where $\omega_E = E_r/B^\theta$ is the $E \times B$ precession frequency. The radial electric field is also large enough that the resonance between $\boldsymbol{v}_E$ and $\boldsymbol{v}_{\mathrm{m}}$ cannot occur, so the superbanana-plateau[24] and superbanana[73] regimes are avoided. This significant E_r may allow bounce-harmonic resonance to occur. The $l = 1$ resonance condition $\omega_b - n(\omega_E + \omega_B) = 0$, will be satisfied for $v_{\parallel} \approx v_{ti}$ with $E_r \sim 7$ kV/m at $r/a = 0.9$, where ω_b is the bounce frequency and ω_B is the toroidal magnetic drift precession.[26] However, we see no evidence of peaking or τ^{NTV} with E_r that would be indicative of a bounce-harmonic resonance.

The banana diffusion $\sqrt{\nu}$ regime becomes relevant when the poloidal $\boldsymbol{E} \times \boldsymbol{B}$ precession frequency is larger than the effective collision frequency of detrapping banana particles, $\nu/\epsilon < \omega_E$, and the ripple magnitude is not large enough for collisionless detrapping to take effect, $\delta_B < \left(\epsilon\nu/\omega_E\right)^{1/2}$. In the collisionless detrapping-retrapping regime, neoclassical fluxes scale with ν.[21] This regime becomes relevant when $\delta_B > \left(\epsilon\nu/\omega_E\right)^{1/2}$ and the perturbing field becomes large enough that poloidally trapped particles can become detrapped and retrapped by the ripple. In the $\sqrt{\nu}$ regime $\tau^{\mathrm{NTV}} \sim \delta_B^2$ and in the ν regime $\tau^{\mathrm{NTV}} \sim \delta_B$. The $1/\nu$ ripple trapping regime predicts $\Gamma_\psi \sim (\delta_B^{3/2})$.[20,30] Stellarator ripple transport in the $\sqrt{\nu}$ regime also predicts $\Gamma_\psi \sim (\delta_B^{3/2})$.[28] For δ_B smaller than $\delta_B^* = 0.82\%$, the actual value of ripple at $r/a = 0.9$ for ITER geometry, the scaling of τ^{NTV} with δ_B is slightly shallower than what is predicted. The departure of the SFINCS calculations from the quasilinear prediction, $\Gamma_\psi \propto \delta_B^2$, indicates the presence of nonlinear effects such as local ripple trapping. The departure from quasilinear scaling increases with δ_B, which is consistent with comparisons of SFINCS with quasilinear NEO-2.[43]
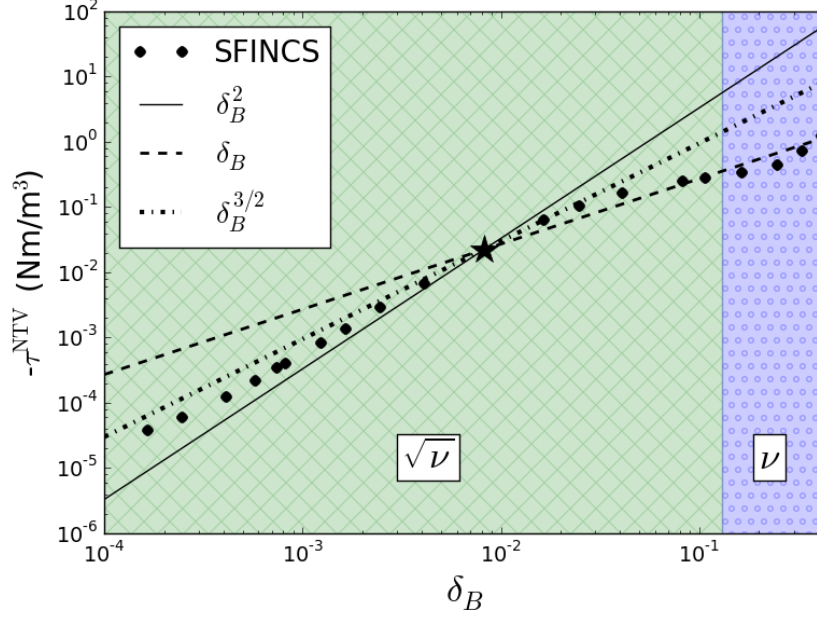
FIG. VII.1. SFINCS calculations of NTV torque density as a function of δ_B at $r/a = 0.9$. A single value of $E_r = 30$ kV/m is used corresponding to the intrinsic rotation estimate. Color-shaded area indicates the approximate regions of applicability for rippled tokamak banana diffusion regimes described by Shaing: the $\sqrt{\nu}$ regime where $\tau^{\mathrm{NTV}} \sim \delta_B^2$ [34] and the ν regime where $\tau^{\mathrm{NTV}} \sim \delta_B$.[21]

VIII. HEAT FLUX CALCULATION

As well as driving non-ambipolar particle fluxes, the breaking of toroidal symmetry drives an additional neoclassical heat flux. In figure VIII.1, the SFINCS calculation of heat flux is shown for three magnetic geometries: (i) axisymmetric (blue solid), (ii) with TF ripple only (green dashed), and (iii) TF ripple with TBMs and FIs (red dash-dot). In the presence of TF ripple, the ripple drives an additional heat flux that is comparable to the axisymmetric heat flux. However, with the addition of the FIs the heat flux is reduced to the magnitude of the axisymmetric value, except near $E_r = 0$ where $1/\nu$ transport dominates.

While the radial ripple-drive particle fluxes will significantly alter the ITER angular momentum transport, the neoclassical heat fluxes are insignificant in comparison to the turbulent heat flux. Note that the neoclassical heat flux is $\lesssim 5\%$ of the heat flux calculated from heating and fusion rate profiles (see appendix B), $Q \approx 0.2$ MW/m². Thus we can attribute $\gtrsim 95\%$ of the heat transport to turbulence. If ITER ripple were scaled up to $\delta_B \gtrsim 30\%$, the

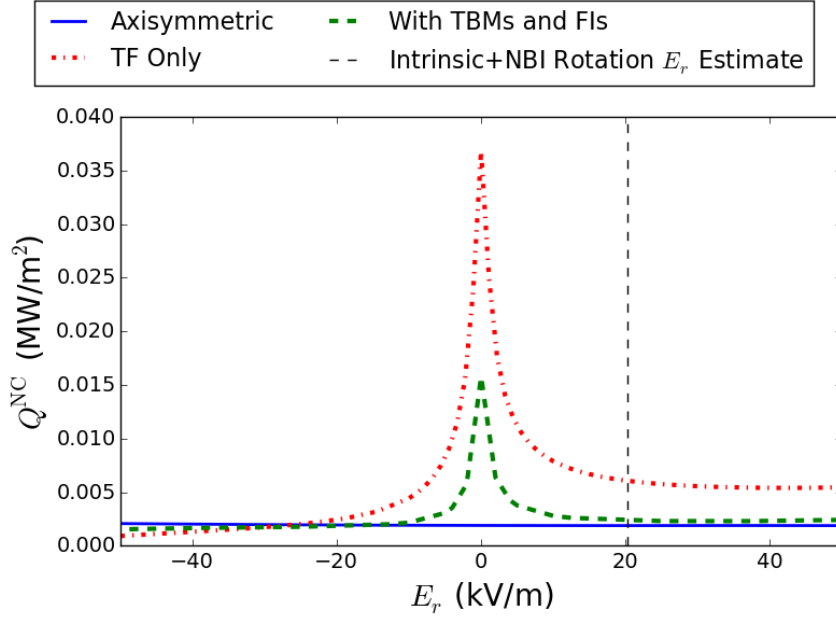neoclassical ripple heat transport would be comparable to the anomalous transport.

FIG. VIII.1.   SFINCS calculation of neoclassical heat flux at $r/a = 0.9$ for three magnetic geometries: (i) axisymmetric (blue solid), (ii) with TF ripple only (green dashed), and (iii) TF ripple with TBMs and FIs (red dash-dot). The vertical dashed line corresponds to the intrinsic and NBI rotation estimate for E_r. These heat fluxes are much smaller than the anomalous heat transport is likely to be, $Q \approx 0.2 \ \mathrm{MW/m^2}$,

IX.   TANGENTIAL MAGNETIC DRIFTS

Although $(\boldsymbol{v}_E + \boldsymbol{v}_\mathrm{m}) \cdot \nabla f_1$ is formally of lower order than the other terms in eq. V.2, it has been found to be important when $\rho_* \sim \nu_*$[74,75] and has been included in other calculations of 3D neoclassical transport. In the SFINCS calculations shown in sections V, VI, VII, and VIII, $\boldsymbol{v}_\mathrm{m} \cdot \nabla f_1$ has not been included. As SFINCS does not maintain radial coupling of f_1, the poloidal and toroidal drifts are retained in this term while the radial drift is not. Note that the radial magnetic drift is retained in $\boldsymbol{v}_\mathrm{m} \cdot \nabla f_0$.

Several issues must be considered when the poloidal and toroidal magnetic drifts are present. A coordinate-dependence can be introduced when the $\boldsymbol{v}_\mathrm{m} \cdot \nabla \psi$ term is ignored, as $\nabla \theta$ and $\nabla \zeta$ do not necessarily lie on the flux surface. For a coordinate-independent form, one

25

must project $\boldsymbol{v}_{\mathrm{m}}$ onto the flux surface. Additionally, when poloidal and toroidal drifts are retained, the effective particle trajectories do not necessarily conserve μ when $\mu = 0$. The drifts can be regularized in order to satisfy $\dot{\xi}(\xi = \pm 1) = 0$ where $\xi = v_{\parallel}/v$. Regularization also eliminates the need for additional particle and heat sources due to the radially local assumption and preserves ambipolarity of axisymmetric systems.[76] To this end, we employ a coordinate-independent magnetic drift perpendicular to $\nabla\psi$,

$$\boldsymbol{v}_{\mathrm{ma}}^{\perp} = \frac{v^2}{2B^2\Omega_a}\frac{(\boldsymbol{B} \times \nabla\psi)}{|\nabla\psi|^2}\nabla\psi \cdot \left[(1 - \xi^2)\nabla B + 2B\xi^2(\boldsymbol{b} \cdot \nabla\boldsymbol{b})\right]. \qquad (IX.1)$$

We note that the ∇B drift term is regularized while the curvature drift term is not. Note that the trapped portion of velocity space is most strongly affected by the addition of $\boldsymbol{v}_m \cdot \nabla f_1$ for which $\xi^2 \ll 1$. For this reason we can drop the curvature drift for regularization,

$$\boldsymbol{v}_{\mathrm{ma}}^{\perp} = \frac{v^2}{2B^2\Omega_a}(\boldsymbol{B} \times \nabla\psi)(1 - \xi^2)\frac{(\nabla\psi \cdot \nabla B)}{|\nabla\psi|^2}. \qquad (IX.2)$$

Note that this is similar to the form presented by Sugama,[76] but we have chosen a different form of regularization. We compare this form with the form of magnetic drifts without projection or regularization,

$$\boldsymbol{v}_{\mathrm{ma}} = \frac{v^2}{2\Omega_a B^2}(1 + \xi^2)\boldsymbol{B} \times \nabla B + \frac{v^2}{\Omega_a B}\xi^2\nabla \times \boldsymbol{B}. \qquad (IX.3)$$

An E_r scan at $r/a = 0.7$, where ρ_* becomes comparable to ν_*, is shown in figure IX.1. When $\boldsymbol{v}_{\mathrm{m}} \cdot \nabla f_1$ is added to the kinetic equation, the typical peak at $E_r = 0$ is shifted toward a slightly negative E_r, corresponding to the region where $(\boldsymbol{v}_E + \boldsymbol{v}_M) \cdot \nabla\zeta \approx 0$. This corresponds to the superbanana-plateau transport regime in which the bounce averaged toroidal drift vanishes. Here the collisionality is large enough that superbananas cannot complete their collisionless trajectories but small enough that non-resonant trapped particles precess, $\nu_*^{\mathrm{SB}} \ll \nu_* \ll \nu_*^{\mathrm{SBP}}$, where $\nu_*^{\mathrm{SBP}} = \rho_* q^2/\epsilon^{1/2}$ and $\nu_*^{SB} = \rho_*\delta_B^{3/2}q^2/\epsilon^2$.[24,73]

We see that when the in-surface magnetic drifts are present the depth of the resonant peak is diminished. In the absence of magnetic drifts the superbanana-plateau resonance can only occur at $E_r = 0$. However, the resonance can occur for all particles regardless of pitch angle and energy. When tangential drifts are added to the DKE, the resonant peak will occur at the E_r for which thermal trapped particles satisfy the resonance condition. However, only particles above a certain energy and at the resonant pitch angle will participate in the

26

superbanana-plateau transport, thus the depth of the peak is diminished. Note that local ripple trapping might also contribute to the $1/\nu$ transport at small E_r. For $|E_r| > 20$ kV/m, the range relevant for ITER, the addition of $\boldsymbol{v}_M \cdot \nabla f_1$ has a negligible effect on τ^{NTV}. The addition of tangential drifts would not dramatically change the results in previous sections.
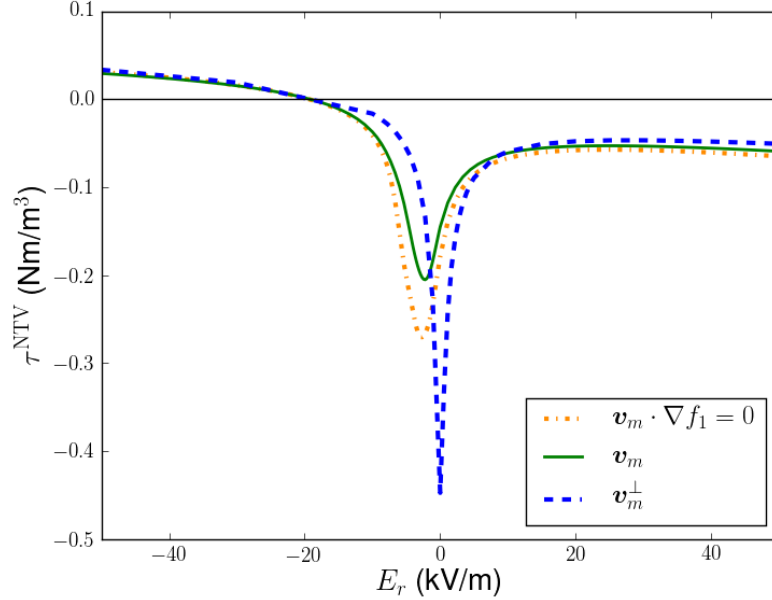

FIG. IX.1. Calculation of NTV torque density, τ^{NTV}, as a function of E_r at $r/a = 0.7$. The orange dash-dot curve corresponds to a SFINCS calculation without $\boldsymbol{v}_m \cdot \nabla f_1$ in the DKE. The green solid curve corresponds to the addition of $\boldsymbol{v}_m \cdot \nabla f_1$ as given in eq. IX.3. The blue dashed curve corresponds to the addition of the projected and regularized drift as given in eq. IX.2.

X. SUMMARY

We calculate neoclassical transport in the presence of 3D magnetic fields, including toroidal field ripple and ferromagnetic components, for an ITER steady state scenario. We use an intrinsic turbulent rotation model described to estimate E_r for neoclassical calculations. We find that even without τ^{NTV}, toroidal rotation will be $\lesssim 2\% \, M_A$, which is likely not large enough to suppress resistive wall modes.[5] We use VMEC free boundary equilibria in the presence of ripple fields to calculate neoclassical particle and heat fluxes using the drift-kinetic solver, SFINCS. At large radii $r/a \gtrsim 0.5$, τ^{NTV} is comparable to τ^{NBI} in magnitude

but opposite in sign, which may result in flow damping at the edge and a decrease in MHD stability. The integral NTV torque, -40 Nm, is larger in magnitude than NBI torque, 35 Nm, so non-resonant magnetic braking cannot be ignored in analysis of ITER rotation. The torque profile may also result in a significant rotation shear which could suppress turbulent transport. While the addition of FIs significantly reduces the transport ($\approx 80\%$ reduction at $r/a = 0.9$), the low n of the TBM ripple produce very little NTV torque. While the NTV torque has been shown to be important for ITER angular momentum balance, iteratively solving for the rotation profile with τ^{NTV} will be left for future consideration.

Appendix A: Parallel Flow is Less Sensitive to Perturbing Field Than Particle Fluxes

In this section we will show that the contribution to $V_{||}$ from f_1 is of order $\nu_* \ll 1$ smaller than the contribution to Γ_ψ. As $V_{||}$ is an odd moment of $v_{||}$ (eq. V.1), only the component of f_1 that is odd in $v_{||}$ will contribute. Similarly, only the component of f_1 that is even in $v_{||}$ will contribute to Γ_ψ as it is an even moment of $v_{||}$ (eq. VI.1). We start with the following DKE,

$$v_{||}\boldsymbol{b} \cdot \nabla f_1 + \boldsymbol{v}_{\mathrm{m}} \cdot \nabla\psi \frac{\partial f_0}{\partial \psi} = C(f_1), \tag{A.1}$$

and perform a secondary expansion of $f_1 = f_1^0 + f_1^1 + ...$ in $\nu_* = \nu_{ii}Rq/(\epsilon^{3/2}v_{ti}) \ll 1$. We use field-aligned coordinates (ψ, θ, ζ_0) where $\zeta_0 = q\theta - \zeta$ and velocity space coordinates (v, μ, σ) where $\sigma = v_{||}/|v_{||}|$. To lowest order we have

$$v_{||}\boldsymbol{b} \cdot \nabla f_1^0 = 0. \tag{A.2}$$

This implies that $f_1^0(\psi, \zeta_0, v, \mu, \sigma)$ in the trapped region and $f_1^0(\psi, \zeta_0, v, \mu, \sigma)$ in the passing region. In the trapped region we must have that $f_{1,t}^0(\sigma = 1, \theta_b) = f_{1,t}^0(\sigma = -1, \theta_b)$ where θ_b is the bounce angle and $\sigma = v_{||}/|v_{||}|$. Therefore, $f_{1,t}^0(\sigma = 1) = f_{1,t}^0(\sigma = -1)$, and $f_{1,t}^0$ is even in $v_{||}$. We next consider the parity of $f_{1,p}^0$ in the passing region of velocity space. The next order equation in ν_* is,

$$v_{||}\boldsymbol{b} \cdot \nabla f_1^1 + \boldsymbol{v}_{\mathrm{m}} \cdot \nabla\psi \frac{\partial f_0}{\partial \psi} = C(f_1^0). \tag{A.3}$$

We apply the transit averaging operation, $\langle...\rangle_t$, to eq. A.3,

$$\langle...\rangle_t = \int_0^{2\pi} \frac{d\theta\, B}{v_\parallel B^\theta}(...),\tag{A.4}$$

which annihilates the left hand side. Let C be a pitch angle scattering operator,

$$C = \frac{\nu v_\parallel}{B} \frac{\partial}{\partial \mu} \left(v_\parallel \mu \frac{\partial}{\partial \mu} \right).\tag{A.5}$$

Performing indefinite integration in μ, we can rewrite eq. A.3 as,

$$f_{1,p}^0(v,\sigma,\mu,\zeta_0) = A(v,\sigma,\zeta_0) + \frac{B(v,\sigma,\zeta_0)}{\int_0^{2\pi} \frac{d\theta v_\parallel}{B^\theta}} \log(\mu)\tag{A.6}$$

For some functions A and B. Because of the divergence at $\mu = 0$ in the second term in eq. A.6, we must have $B = 0$. As f_1^0 must be continuous across the trapped-passing boundary, $f_{1,p}^0$ cannot be a function of σ and must also have even parity in $v_\parallel$. We can solve eq. A.3 for f_1^1 by performing indefinite integration in θ.

$$f_1^1 = \int \frac{d\theta B}{B^\theta v_\parallel} \left[C(f_1^0) - \boldsymbol{v}_\mathrm{m} \cdot \nabla\psi \frac{\partial f_0}{\partial \psi} \right] + D(\psi,\zeta_0,v,\sigma,\mu),\tag{A.7}$$

for some function D. Within the integrand, $C(f_1^0)$ can be rewritten by expanding f_1^0 in even Legendre polynomials in ξ, $f_1^0 = \sum_{\mathrm{even}\, l} f_{1,l}^0 P_l(\xi)$,

$$C(f_1^0) = \sum_{\mathrm{even}\, l} l(l+1) f_{1,l}^0 P_l(\xi).\tag{A.8}$$

So $C(f_1^0)$ will have the same parity as f_1^0. As both $C(f_1^0)$ and $\boldsymbol{v}_\mathrm{m} \cdot \nabla\psi$ are even in $v_\parallel$, f_1^1 will have a component odd in parity and will contribute to $V_\parallel$. Therefore, the departure of $V_\parallel$ from the axisymmetric value will occur at order ν_* higher than the departure of Γ_ψ from its axisymmetric value.

Appendix B: Approximate Turbulent Heat Flux and Torque

As Π_int is proportional to Q in our model, we must estimate Q using the input heating power and D-T fusion rates calculated with TRANSP and TSC. The LH, NBI, and ECH power densities (P_LH, P_NBI, and P_ECH) are integrated along with the fusion reaction rate density (R_DT) to calculate the total integrated heating source, $H(r)$,

$$\int_0^r dV\, H(r) = \int_0^r dV \left(P_\mathrm{LH} + P_\mathrm{NBI} + P_\mathrm{ECH} + R_\mathrm{DT}(3.5\mathrm{MeV}) \right).\tag{B.1}$$

As $\int Q dS = \int H dV$,

$$Q(r) = \frac{\int_0^{V(r)} dV' \left(P_{\text{LH}} + P_{\text{NBI}} + P_{\text{ECH}} + R_{\text{DT}}(3.5\text{MeV}) \right)}{A(r)}, \tag{B.2}$$

where $A(r) = V'(r)$ is the flux surface area. We have shown in section VIII that the neoclassical heat flux is insignificant in comparison to $Q(r)$, so we can attribute $Q(r)$ to turbulent heat transport. The calculated Q is shown in figure B.1.
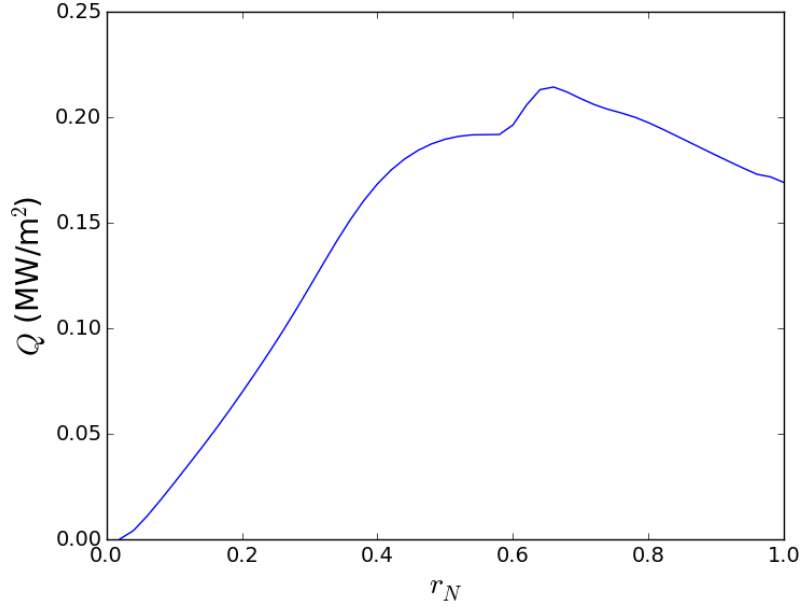

FIG. B.1. Heat flux Q calculated with input heating and fusion rate profiles from TRANSP and TSC.

We estimate $\tau^{\text{turb}} = -\nabla \cdot \Pi_{\text{int}} \sim -\Pi_{\text{int}}/a$ using

$$\Pi_{\text{int}} \sim \frac{\rho_\theta \widetilde{\Pi}(\nu_*) Q \langle R \rangle}{v_{ti} L_T}. \tag{B.3}$$

The quantity τ^{turb} is shown in figure VI.5.

ACKNOWLEDGEMENTS

REFERENCES

[1] A. Bondeson and D. J. Ward, Physical Review Letters **72**, 2709 (1994).

[2] A. M. Garofalo, E. J. Strait, L. C. Johnson, R. J. La Haye, E. A. Lazarus, G. A. Navratil, M. Okabayashi, J. T. Scoville, T. S. Taylor, and A. D. Turnbull, Physical Review Letters **89**, 235001 (2002).

[3] K. H. Burrell, Physics of Plasmas **4**, 1499 (1997).

[4] P. W. Terry, Reviews of Modern Physics **72**, 109 (2000).

[5] Y. Liu, A. Bondeson, Y. Gribov, and A. Polevoi, Nuclear Fusion **44**, 232 (2004).

[6] M. Hua, I. T. Chapman, A. R. Field, R. J. Hastie, S. D. Pinches, and the MAST Team, Plasma Physics and Controlled Fusion **52**, 035009 (2010).

[7] E. Lazzaro, R. J. Buttery, T. C. Hender, P. Zanca, R. Fitzpatrick, M. Bigi, T. Bolzonella, R. Coelho, M. DeBenedetti, S. Nowak, O. Sauter, and M. Stamp, Physics of Plasmas **9**, 3906 (2002).

[8] P. de Vries, A. Salmi, V. Parail, C. Giroud, Y. Andrew, T. Biewer, K. Crombé, I. Jenkins, T. Johnson, V. Kiptily, A. Loarte, J. Lönnroth, A. Meigs, N. Oyama, R. Sartori, G. Saibene, H. Urano, K. Zastrow, and JET EFDA contributors, Nuclear Fusion **48**, 035007 (2008).

[9] S. M. Wolfe, I. H. Hutchinson, R. S. Granetz, J. Rice, A. Hubbard, A. Lynn, P. Phillips, T. C. Hender, D. F. Howell, R. J. La Haye, and J. T. Scoville, Physics of Plasmas **12**, 1 (2005).

[10] A. M. Garofalo, K. H. Burrell, J. C. Deboo, J. S. Degrassie, G. L. Jackson, M. Lanctot, H. Reimerdes, M. J. Schaffer, W. M. Solomon, and E. J. Strait, Physical Review Letters **101** (2008).

[11] H. Reimerdes, Nuclear Fusion **49**, 115001 (2009).

[12] M. Honda, S. Satake, Y. Suzuki, G. Matsunaga, K. Shinohara, M. Yoshida, A. Matsuyama, S. Ide, and H. Urano, Nuclear Fusion **54**, 114005 (2014).

[13]W. Zhu, S. A. Sabbagh, R. E. Bell, J. M. Bialek, M. G. Bell, B. P. Leblanc, S. M. Kaye, F. M. Levinton, J. E. Menard, K. C. Shaing, A. C. Sontag, and H. Yuh, Physical Review Letters **96**, 1 (2006).

[14]V. A. Chuyanov, D. J. Campbell, and L. M. Giancarli, Fusion Engineering and Design **85**, 2005 (2010).

[15]M. Schaffer, J. Snipes, P. Gohil, P. de Vries, T. Evans, M. Fenstermacher, X. Gao, A. Garofalo, D. Gates, C. Greenfield, W. Heidbrink, G. Kramer, R. La Haye, S. Liu, A. Loarte, M. Nave, T. Osborne, N. Oyama, J. Park, N. Ramasubramanian, H. Reimerdes, G. Saibene, A. Salmi, K. Shinohara, D. Spong, W. Solomon, T. Tala, Y. Zhu, J. Boedo, V. Chuyanov, E. Doyle, M. Jakubowski, H. Jhang, R. Nazikian, V. Pustovitov, O. Schmitz, R. Srinivasan, T. Taylor, M. Wade, K. You, and L. Zeng, Nuclear Fusion **51**, 103028 (2011).

[16]M. Lanctot, J. Snipes, H. Reimerdes, C. Paz-Soldan, N. Logan, J. Hanson, R. Buttery, J. DeGrassie, A. Garofalo, T. Gray, B. Grierson, J. King, G. Kramer, R. La Haye, D. Pace, J.-K. Park, A. Salmi, D. Shiraki, E. Strait, W. Solomon, T. Tala, and M. Van Zeeland, Nuclear Fusion **57**, 036004 (2017).

[17]K. Tobita, T. Nakayama, S. V. Konovalov, and M. Sato, Plasma Physics and Controlled Fusion **45**, 133 (2003).

[18]H. Urano, N. Oyama, K. Kamiya, Y. Koide, H. Takenaga, T. Takizuka, M. Yoshida, Y. Kamada, and the JT-60 Team, Nuclear Fusion **47**, 706 (2007).

[19]H. Kawashima, M. Sato, K. Tsuzuki, Y. Miura, N. Isei, H. Kimura, T. Nakayama, M. Abe, D. Darrow, and J.-M. Group, Nuclear Fusion **41**, 257 (2001).

[20]T. E. Stringer, Nuclear Fusion **12**, 689 (1972).

[21]K. C. Shaing, S. A. Sabbagh, and M. S. Chu, Plasma Physics and Controlled Fusion **51**, 035004 (2009).

[22]K. Shaing and J. Callen, Nuclear Fusion **22**, 1061 (1982).

[23]K. C. Shaing and J. D. Callen, Physics of Fluids **25**, 1012 (1982).

[24]K. C. Shaing, S. A. Sabbagh, and M. S. Chu, Plasma Physics and Controlled Fusion **51**, 035009 (2009).

[25]R. Linsker and A. H. Boozer, Phys. Fluids **25**, 143 (1982).

[26]J. K. Park, A. H. Boozer, J. E. Menard, A. M. Garofalo, M. J. Schaffer, R. J. Hawryluk, S. M. Kaye, S. P. Gerhardt, and S. A. Sabbagh, Physics of Plasmas **16** (2009).

[27] A. Galeev and R. Sagdeev, Physical Review Letters **22**, 511 (1969).

[28] D. D. Ho and R. M. Kulsrud, Physics of Fluids **30**, 442 (1987).

[29] E. A. Frieman, Physics of Fluids **13**, 490 (1970).

[30] J. Connor and R. Hastie, Nuclear Fusion **13**, 221 (1973).

[31] L. Kovrizhnykh, Nuclear Fusion **24**, 851 (1984).

[32] J. N. Davidson, Nuclear Fusion **16**, 731 (1976).

[33] K. C. Shaing, Physics of Plasmas **10**, 1443 (2003).

[34] K. C. Shaing, P. Cahyna, M. Becoulet, J. K. Park, S. A. Sabbagh, and M. S. Chu, Physics of Plasmas **15** (2008).

[35] K. Shaing, S. Sabbagh, and M. Chu, Nuclear Fusion **50**, 025022 (2010).

[36] S. C. Jardin, N. Ferraro, X. Luo, J. Chen, J. Breslau, K. E. Jansen, and M. S. Shephard, Journal of Physics: Conference Series **125**, 012044 (2008).

[37] S. P. Hirshman, K. C. Shaing, W. I. van Rij, C. O. Beasley, and E. C. Crume, Physics of Fluids **29**, 2951 (1986).

[38] N. M. Ferraro, S. C. Jardin, and P. B. Snyder, Physics of Plasmas **17** (2010).

[39] A. J. Cole, J. D. Callen, W. M. Solomon, A. M. Garofalo, C. C. Hegna, M. J. Lanctot, and H. Reimerdes, Physics of Plasmas **18** (2011), 10.1063/1.3590933.

[40] Y. Sun, Y. Liang, K. C. Shaing, H. R. Koslowski, C. Wiegmann, and T. Zhang, Physical Review Letters **105** (2010), 10.1103/PhysRevLett.105.145002.

[41] S. Satake, H. Sugama, R. Kanno, and J.-K. Park, Plasma Physics and Controlled Fusion **53**, 054018 (2011).

[42] S. Satake, J. K. Park, H. Sugama, and R. Kanno, Physical Review Letters **107**, 1 (2011).

[43] A. F. Martitsch, S. V. Kasilov, W. Kernbichler, G. Kapper, C. G. Albert, M. F. Heyn, H. M. Smith, E. Strumberger, S. Fietz, W. Suttrop, and M. Landreman, Plasma Physics and Controlled Fusion **58**, 074007 (2016).

[44] M. Landreman, H. M. Smith, A. Mollén, and P. Helander, Physics of Plasmas **21** (2014).

[45] S. Hirshman, W. van Rij, and P. Merkel, Computer Physics Communications **43**, 143 (1986).

[46] W. I. van Rij and S. P. Hirshman, Physics of Fluids B: Plasma Physics **1**, 563 (1989).

[47] D. Ćirić, A. D. Ash, B. Crowley, I. E. Day, S. J. Gee, L. J. Hackett, D. A. Homfray, I. Jenkins, T. T. C. Jones, D. Keeling, D. B. King, R. F. King, M. Kovari, R. McAdams,

E. Surrey, D. Young, and J. Zacks, Fusion Engineering and Design **86**, 509 (2011).

[48]F. I. Parra, M. F. F. Nave, A. A. Schekochihin, C. Giroud, J. S. De Grassie, J. H. F. Severo, P. De Vries, and K. D. Zastrow, Physical Review Letters **108**, 1 (2012).

[49]J. Rice, A. Ince-Cushman, J. DeGrassie, L. Eriksson, Y. Sakamoto, A. Scarabosio, A. Bortolon, K. Burrell, B. Duval, C. Fenzi-Bonizec, M. Greenwald, R. Groebner, G. Hoang, Y. Koide, E. Marmar, A. Pochelon, and Y. Podpaly, Nuclear Fusion **47**, 1618 (2007).

[50]J. S. DeGrassie, J. E. Rice, K. H. Burrell, R. J. Groebner, and W. M. Solomon, Physics of Plasmas **14** (2007).

[51]J. M. Noterdaeme, E. Righi, V. Chan, J. DeGrassie, K. Kirov, M. Mantsinen, M. F. F. Nave, D. Testa, K. D. Zastrow, R. Budny, R. Cesario, A. Gondhalekar, N. Hawkes, T. Hellsten, P. Lamalle, F. Meo, F. Nguyen, and the EFDA-JET-EFDA Contributors, Nuclear Fusion **43**, 274 (2003).

[52]M. Barnes, F. I. Parra, J. P. Lee, E. A. Belli, M. F. F. Nave, and A. E. White, Physical Review Letters **111**, 1 (2013).

[53]F. Poli, C. Kessel, P. Bonoli, D. Batchelor, R. Harvey, and P. Snyder, Nuclear Fusion **54**, 073007 (2014).

[54]S. C. Jardin, N. Pomphrey, and J. Delucia, Journal of Computational Physics **66**, 481 (1986).

[55]R. Hawryluk, Physics of plasmas close to thermonuclear conditions **1**, 19 (1980).

[56]S. C. Jardin, M. G. Bell, and N. Pomphrey, Nuclear Fusion **33**, 371 (1993).

[57]P. Snyder, R. Groebner, J. Hughes, T. Osborne, M. Beurskens, A. Leonard, H. Wilson, and X. Xu, Nuclear Fusion **51**, 103016 (2011).

[58]K. Shinohara, T. Oikawa, H. Urano, N. Oyama, J. Lonnroth, G. Saibene, V. Parail, and Y. Kamada, Fusion Engineering and Design **84**, 24 (2009).

[59]M. N. Rosenbluth and F. L. Hinton, Nuclear Fusion **36**, 55 (1996).

[60]J. Hillesheim, F. Parra, M. Barnes, N. Crocker, H. Meyer, W. Peebles, R. Scannell, and A. Thornton, Nuclear Fusion **55**, 032003 (2015).

[61]J. W. Berkery, S. A. Sabbagh, R. Betti, B. Hu, R. E. Bell, S. P. Gerhardt, J. Manickam, and K. Tritz, Physical Review Letters **104**, 1 (2010).

[62]Y. Liu, M. Chu, I. T. Chapman, and T. Hender, Nuclear Fusion **49**, 035004 (2009).

[63]L. Hinton and R. D. Hazeltine, Reviews of Modern Physics **48**, 239 (1976).

[64]S. Hirshman and D. Sigmar, Nuclear Fusion **21**, 1079 (1981).

[65]J. Callen, Nuclear Fusion **51**, 094026 (2011).

[66]Y. Sun, Y. Liang, K. Shaing, H. Koslowski, C. Wiegmann, and T. Zhang, Nuclear Fusion **51**, 053015 (2011).

[67]C. G. Albert, M. F. Heyn, G. Kapper, S. V. Kasilov, W. Kernbichler, and A. F. Martitsch, Physics of Plasmas **23** (2016).

[68]K. C. Shaing, Physics of Fluids **29**, 2231 (1986).

[69]K. C. Shaing, Physics of Plasmas **13**, 10 (2006).

[70]X. Garbet, J. Abiteboul, E. Trier, Ö. Gürcan, Y. Sarazin, A. Smolyakov, S. Allfrey, C. Bourdelle, C. Fenzi, V. Grandgirard, P. Ghendrih, and P. Hennequin, Physics of Plasmas **17** (2010).

[71]J. W. Connor and R. J. Hastie, Physics of Fluids **17**, 114 (1974).

[72]T. S. Hahm, Physics of Plasmas **1**, 2940 (1994).

[73]K. C. Shaing, S. A. Sabbagh, and M. S. Chu, Plasma Physics and Controlled Fusion **51**, 055003 (2009).

[74]I. Calvo, F. I. Parra, J. L. Velasco, and J. A. Alonso, (2016), 1610.06016.

[75]S. Matsuoka, S. Satake, R. Kanno, and H. Sugama, Physics of Plasmas **22** (2015).

[76]H. Sugama, S. Matsuoka, S. Satake, and R. Kanno, Physics of Plasmas **23**, 042502 (2016).